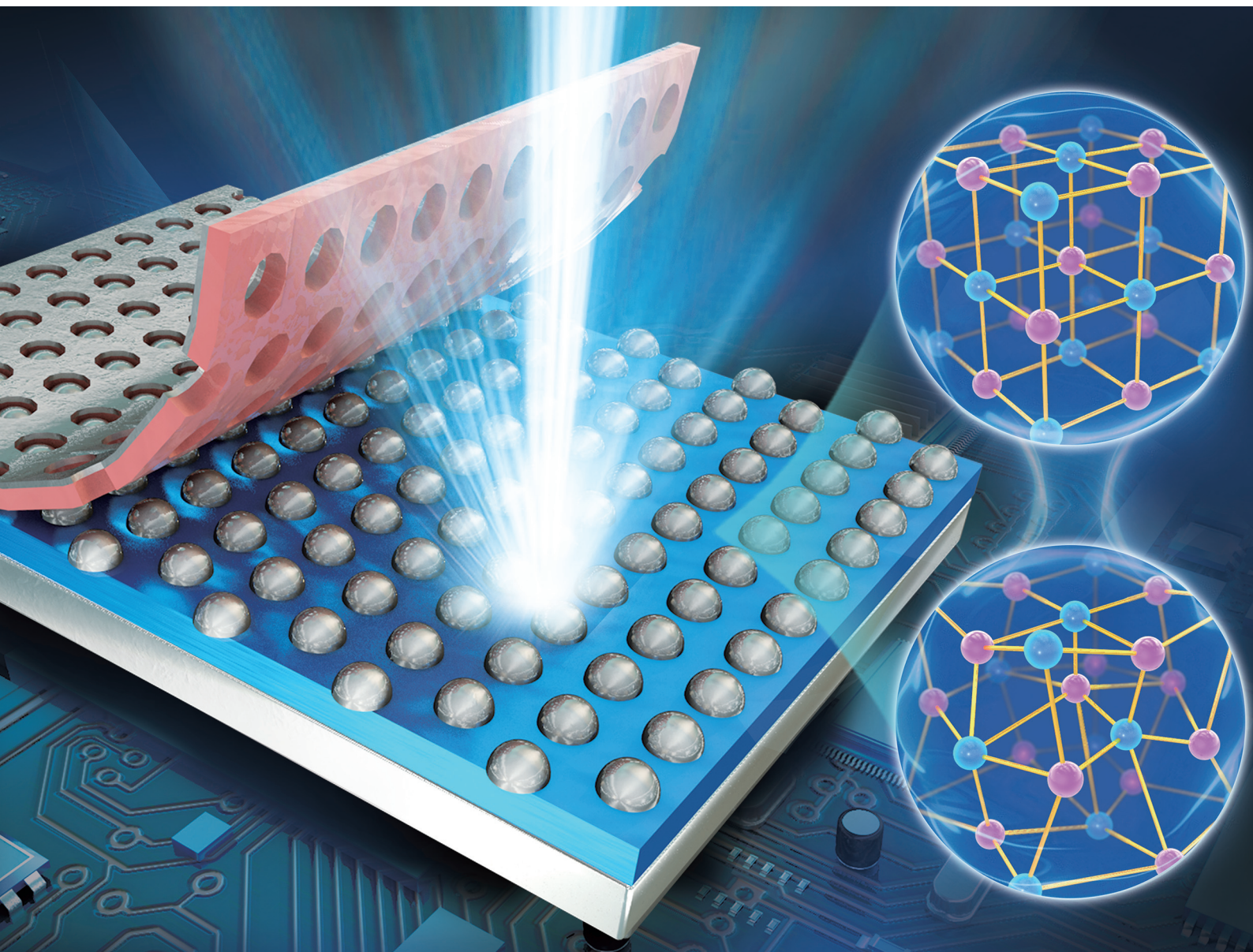


Nanoscale

rsc.li/nanoscale



ISSN 2040-3372

PAPER

Long Zhang, Shulin Sun *et al.*
Large-scale, low-cost, broadband and tunable perfect
optical absorber based on phase-change material



Cite this: *Nanoscale*, 2020, **12**, 5374

Large-scale, low-cost, broadband and tunable perfect optical absorber based on phase-change material†

Nanli Mou,^{a,b} Xiaolong Liu,^c Tao Wei,^a Hongxing Dong,^a Qiong He,^{d,e} Lei Zhou,^{d,e} Yaqiang Zhang,^{a,b} Long Zhang^{✉*} and Shulin Sun^{✉*}

Metamaterial-based electromagnetic absorbers have attracted much attention recently, but most previous realizations suffer from issues of narrow bandwidth, time-consuming and high-cost fabrication methods, and/or fixed functionalities, and so are unfavorable for practical applications. Here, we demonstrate experimentally a large-scale, broadband, polarization-independent, and tunable metamaterial absorber, which works for both visible and near-infrared light. A lithography-free and low-cost method was utilized to fabricate a centimeter-sized metamaterial sample in a metal–insulator–metal (MIM) configuration with nano-scale precision, in which a phase-change material, Ge₂Sb₂Te₅ (GST), was adopted as the insulating spacer of the MIM structure. With two different resonance mechanisms working together, the proposed device was shown to exhibit high absorptivity (>80%) within a broad wavelength band (480–1020 nm). By thermally tuning the phase state of the GST layer, we can dramatically enlarge the working bandwidth of the metamaterial absorber by shifting one absorption peak by about 470 nm. These findings may stimulate many potential applications in, for example, solar cells, energy harvesting, smart sensing/imaging, and color printing.

Received 3rd September 2019,
Accepted 16th January 2020

DOI: 10.1039/c9nr07602f

rsc.li/nanoscale

Introduction

Perfect absorption of electromagnetic (EM) energy plays a vital role in a wide range of applications, such as solar cells, photonic/thermal imaging, sensors, radiative cooling and thermal emitters.^{1–9} However, absorbers made using natural materials suffer from the impedance-mismatch problem due to a lack of magnetic responses, and thus they cannot completely suppress the light reflections that degrade their light-absorbing abilities. Absorbers with taper-like structures^{10,11} can exhibit

gradually varying impedance, and therefore achieve high absorptivity *via* suppressing these reflections. Although these EM absorbers usually operate over broad bandwidths, unfortunately, they exhibit non-flat configurations and bulky sizes, and so are unfavorable for integrated optics applications.

Recently, metamaterial-based EM absorbers have attracted much attention owing to the many unprecedented characteristics that they possess, such as high absorptivity, ultrathin thickness, scalable working wavelength, and/or flat configurations.^{12–16} In 2008, Landy *et al.* proposed a perfect metamaterial EM absorber exhibiting both electric and magnetic responses. Through tailoring of the effective permittivity and permeability of the metamaterial layer, the authors could make the impedance of the structure perfectly match that of air, and thus suppress EM wave reflections, so finally realizing near-perfect absorption of EM waves at certain frequencies. Such metamaterial absorbers were soon realized in reflection geometries,⁷ typically in metal–insulator–metal (MIM) configurations consisting of a layer of metallic microstructures and a continuous metallic mirror separated by a dielectric spacer. Different from the metamaterial absorbers realized in transmission geometry, such MIM absorbers naturally block the transmission channel and thus are much easier to design. Coupling between two metallic layers can generate a magnetic resonance inside an MIM structure,

^aKey Laboratory of Materials for High-Power Laser, Shanghai Institute of Optics and Fine Mechanics, Chinese Academy of Sciences, Shanghai, 201800, China.

E-mail: lzhang@siom.ac.cn

^bCenter of Materials Science and Optoelectronics Engineering, University of Chinese Academy of Sciences, Beijing, 100049, China

^cShanghai Engineering Research Center of Ultra-Precision Optical Manufacturing, Green Photonics and Department of Optical Science and Engineering, Fudan University, Shanghai 200433, China. E-mail: sls@fudan.edu.cn

^dState Key Laboratory of Surface Physics and Key Laboratory of Micro and Nano Photonic Structures (Ministry of Education), Fudan University, Shanghai 200433, China

^eCollaborative Innovation Center of Advanced Microstructures, Nanjing 210093, China

†Electronic supplementary information (ESI) available. See DOI: 10.1039/c9nr07602f

which helps to solve the impedance-matching issue, and, in turn, realizes perfect absorption of EM waves *via* eliminating the reflections at the device surface under certain conditions. Thanks to the simplicity of the working mechanism and the structure, such reflection-type absorbers were soon realized in various frequency domains by scaling the dimensions of the microstructures.⁶ These absorbers are of high working efficiencies, ultrathin thicknesses, and flat configurations, all highly desirable characteristics in integrated optics applications.

Despite this impressive progress, however, most metamaterial absorbers realized so far still suffer from several issues that hinder their practical application, such as narrow bandwidth, fixed working band, and time-consuming and high-cost fabrication methods. Many efforts have been devoted to overcoming these issues. For instance, the bandwidths of absorbers can be enlarged by incorporating multiple resonators with different dimensions,^{17–19,41} or multilayer structures,^{11,20–22} into the metamaterial structures. Unfortunately, these devices are usually of low efficiency and exhibit complicated structures. High-loss metals, such as tungsten, nickel and titanium, were also widely adopted to achieve broadband absorption.^{38–40} However, the fabrication techniques adopted in these studies (for example, electron beam lithography and focused ion beam) are still high cost and low throughput. Meanwhile, tunable metamaterial absorbers with incorporated graphene^{23–25} or phase-change materials (PCMs)^{3,26–28} were also widely investigated. In particular, thermally tunable meta-devices attracted much attention due to some practical applications, such as tunable antireflection, thermal emission, and so on.^{3,36,45,46} However, the tuning ranges of these metamaterial absorbers usually only cover a certain frequency band, which is restricted by the properties of the tunable materials. Ultrathin metamaterial absorbers with working frequencies that are freely tuned inside a broad range covering both visible and near-infrared domains are rarely seen.

In this paper, we demonstrate experimentally a large-scale, broadband, polarization-insensitive and tunable optical metamaterial absorber realized using a low-cost, time-saving and lithography-free fabrication method. Utilizing an aluminum oxide (AAO) nanomask,^{29–34} we successfully deposited aluminum (Al) nanoparticles (NPs) on an ultrathin Ge₂Sb₂Te₅ (GST) layer grown on a continuous metallic mirror, constituting an ultrathin MIM structure with centimeter-scale total size. Through careful design, we can overlap the Fabry–Perot (FP) resonance of the GST film with the localized surface plasmon resonances (LSPR) of the Al NPs, and thus achieve high light absorptivity (>80%) within a broad frequency band covering both the visible and near-infrared regions. Moreover, the bandwidths of these metamaterial absorbers can be dramatically tuned by varying the annealing temperature of the GST layer. Full-wave simulations are in perfect agreement with the optical measurements. Our results could find potential applications in energy harvesting, smart sensing/imaging, and color printing.

Results and discussion

We successfully fabricated a centimeter-scale and high-quality metamaterial absorber utilizing a low-cost and time-saving fabrication method, as depicted schematically in Fig. 1(a). We first deposited a 100 nm-thick Al film on a silica substrate serving as a mirror to eliminate light transmission. A 40 nm-thick GST film was sequentially deposited onto the Al film by a radiofrequency sputtering method. Next, Al nanoparticles were formed on the GST film *via* deposition of an Al thin film through the air-hole array of the AAO mask placed on the GST. We finally obtained a MIM-type metamaterial structure through a lift-off process of the AAO. Such a lithography-free technique allows us to fabricate centimeter-scale nanoparticle arrays with high precision. Fig. 1(b) depicts the SEM image of a typical fabricated sample in a 30° tilted view, with part of the AAO template remaining on the sample. In order to clearly illustrate the configuration of the top Al NPs, the sample was cut along the *z* direction, with its cross-section depicted in Fig. 1(c). It should be noted that, since part of the Al will stick to the side walls of the air holes in the AAO template during the deposition process, the fabricated Al NPs possess a semi-ellipsoidal shape, instead of an ideal cylinder shape. The absorbers with a hemispherical configuration exhibit an additional benefit of broader bandwidth due to their gradually varying dimensions.^{18,30,43} Scanning electron microscopy (SEM) images in Fig. 1(b) and (c) clearly show that the Al NPs array exhibits a hexagonal lattice with a period of about

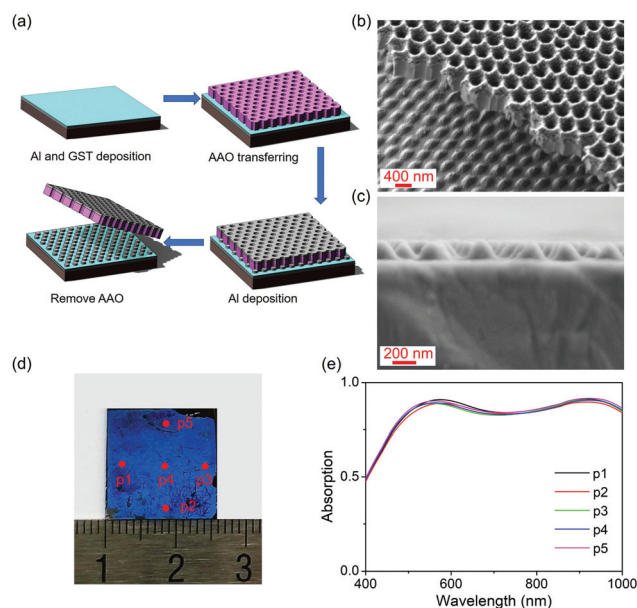


Fig. 1 (a) Fabrication process for the proposed broadband and tunable metamaterial absorber. (b and c) Tilted-view and side-view SEM images of the fabricated absorber samples and part of the AAO mask left on it. (d) Optical photograph of the whole fabricated device taken in a natural white light environment. (e) The measured absorption spectra taken at five different lateral locations on the sample, marked as p1–p5 in (d).

450 nm, while the diameters of the NPs are about 280 nm. Fig. 1(d) illustrates the overall morphology of the fabricated sample (the dark blue area in the image), with a large size (about $1.5 \times 1.5 \text{ cm}^2$). To verify the robust performance of the fabricated sample, we measured the reflection spectra at five different lateral positions on the sample surface (marked as p1–p5 in Fig. 1(d)). Considering that the bottom Al film can eliminate transmission completely, the absorptivity, A , of the present device can be simply obtained from $A = 1 - R$ (where R is the measured reflectivity). Clearly, all measured spectra coincide with each other, showing a broad absorption band ranging from the visible to near-infrared region, as depicted in Fig. 1(e). These measurements demonstrate that such a time-saving and lithography-free method can be a promising approach to fabricate large-scale, high-throughput and low-cost optical metamaterial absorbers.

Having seen the good performance of our fabricated sample, we next discuss the working mechanism of our device, and, in particular, how to design high-performance optical absorbers with such a specific configuration (Fig. 2(a)). For simplicity, we assume that the top layer of our absorber consists of semi-ellipsoid-shaped metallic NPs arranged in an ideal hexagonal lattice, while the bottom layer is a 100 nm-thick continuous Al film. Since the GST film can be tuned between amorphous and crystalline phases by controlling the annealing temperature in the fabrication process, we model this as a dielectric spacer with a refractive index (including

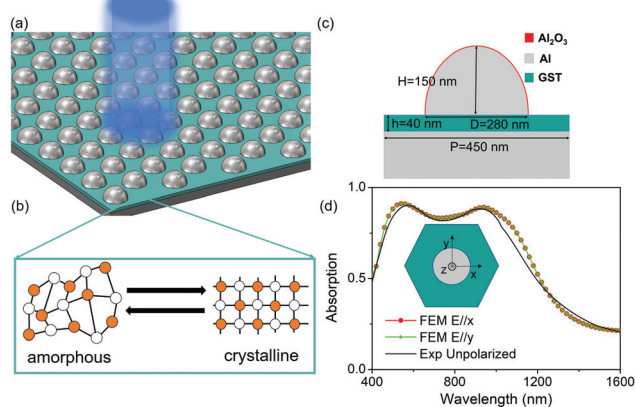


Fig. 2 (a) Schematic of the broadband and tunable metamaterial absorber, which consists of semi-ellipsoidal-shaped aluminum (Al) nanoparticles (NPs) arrayed in a hexagonal lattice, and a continuous Al mirror separated by an ultrathin GST film. (b) Schematic of the phase transition effect from the amorphous state to the crystalline state (or vice versa) for the GST layer. (c) Schematic of one unit cell of the absorber with the Al NPs covered by 2 nm-thick Al_2O_3 shells. The thickness of the bottom GST and Al NPs is $h = 40 \text{ nm}$ and $H = 150 \text{ nm}$, respectively. The lattice constant of the hexagonally arranged Al NPs is $P = 450 \text{ nm}$, and the lateral dimension of the semi-ellipsoidal-shaped Al NPs is $D = 280 \text{ nm}$. (d) Calculated absorption spectra of the broadband absorber normally illuminated by both x-polarized (red dotted line) and y-polarized (green dotted line) incident light, showing good agreement with the experimental result (black). The inset shows the top view of the proposed structure with the GST film being in an amorphous phase.

both the real and imaginary parts) that continuously varies with temperature. Therefore, the proposed metamaterial absorber can exhibit thermally tunable performance. Fig. 2(c) depicts the geometric parameters of the experimentally realized metamaterial absorber with high efficiency and broadband performance. Considering the oxidization effect of Al upon exposure to air, all the Al NPs are covered by 2 nm-thick Al_2O_3 shells in our simulation model. The total thickness of the proposed absorber is only around 300 nm, making it a suitable ultrathin, smart antireflection coating for practical applications. Fig. 2(d) shows both the measured and simulated absorption spectra for the designed absorber, exhibiting a broad absorption band from about 480 to 1020 nm, with an absorptivity above 80%. To achieve this broadband effect, the performance of the proposed absorbers is sacrificed slightly. Therefore, we chose 80% absorptivity as the criterion to define the working band.^{35,44} The absorption spectra for two different polarizations (see the red and green dotted lines in Fig. 2(d)) coincide well with each other, clearly demonstrating the polarization-independent performance of our fabricated sample.

Now that our finite element method (FEM) simulations can reproduce the experimental results well, we continued to explore the underlying physics of the broadband performance of our device, based on these FEM simulations. We find that the key reason for the broadband performance is that two different resonance mechanisms are purposely incorporated into the design/realization of our metamaterial absorber. Fig. 3 depicts the simulated magnetic field intensity (color map) and electric field vector (black arrow) distributions at the wavelengths of two absorption peaks, *i.e.* 540 nm and 940 nm (see Fig. 2(d)). At a wavelength of $\lambda = 540 \text{ nm}$, both the electric and magnetic fields (see color map and arrows) are concentrated mainly around the two poles of the Al NPs in the air layer, verifying that this absorption peak results from the LSPRs of the Al NPs.³⁵ It should be noted that both the diameter, D , and the height, H , of the hemispherical NPs can influence the LSPR. In our design, usually we first fix the diameter of the hemispherical NPs and then finely tune the height of the nanoparticles to make the LSPR locate at the desired wavelength. Conversely, at a wavelength of $\lambda = 940 \text{ nm}$, the magnetic field is confined mainly inside the GST layer, which is consistent with the features of FP resonance.³⁶

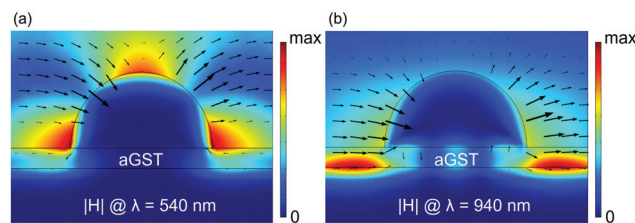


Fig. 3 Simulated magnetic field (colour map) and electric field (black arrows) distributions at the two absorption peaks in Fig. 2(d). To achieve broadband absorption, the LSPR (a) and FP (b) resonances are both utilized in our device.

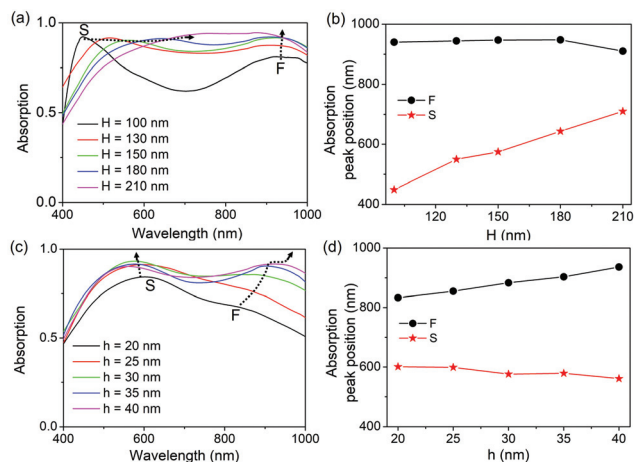


Fig. 4 (a and c) Measured absorption spectra of the fabricated broadband absorber with five different heights, H , for the Al NPs (a) or different GST film thicknesses, h (c), respectively. (b and d) The corresponding wavelengths of two absorption peaks S and F shown in (a and c) as a function of H (b) or h (d).

The absorption band can be freely manipulated by changing the dimensions of the proposed metamaterial absorber. For instance, we can control the height, H , of the top Al NPs by changing the deposition time of Al in the thermal evaporation process. In our experiments, five samples with different H were fabricated, and their measured absorption spectra are depicted in Fig. 4(a). It should be noted that the position of the low-frequency absorption peak (denoted as peak F) remains almost unchanged. Conversely, the high-frequency absorption peak (denoted as peak S) redshifts with increase in H . The resonance wavelengths of these two absorption peaks are shown in Fig. 4(b) as a function of H , clearly revealing these different trends.

We can also manipulate the absorption bandwidth by varying the thickness, h , of the GST layer, as shown in Fig. 4(c). Compared with the cases in Fig. 4(a) and (b), the absorption peak S is nearly fixed, which is reasonable because the local field of the LSPR mode is mainly distributed in air and is thus insensitive to the thickness, h , of the GST layer. Conversely, peak F exhibits a nearly linear redshift with increase in h , further demonstrating the FP nature of the resonance associated with this absorption peak.

Benefiting from the thermally controlled optical properties of the PCMs utilized in our device, we can efficiently tune the working band of the proposed metamaterial absorber by varying the temperature, as demonstrated in Fig. 5. While the as-deposited GST is switched from an amorphous (denoted by aGST) to a crystalline phase (denoted by cGST) state in a 60-minute annealing process at 160 °C, its refractive index exhibits a dramatic change, leading to the tunable absorption property. Fig. 5(a) depicts the measured absorption spectra of the metamaterial absorbers in amorphous (black) and crystalline phases (red), respectively, and showing good agreement with simulation results (dotted line). Clearly, as GST transforms from the amorphous to the crystalline phase, both the real part (n) and the imaginary part (k) of its refractive index

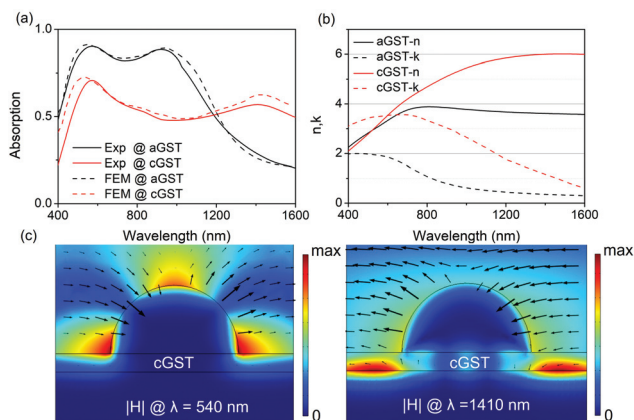


Fig. 5 (a) Measured (solid line) and simulated (dotted line) absorption spectra of the tunable broadband absorber with the GST layer being in amorphous (aGST, black lines) and crystalline (cGST, red lines) states, respectively. (b) The real part, n , and the imaginary part, k , of the refractive index of the GST material at amorphous and crystalline states, respectively. (c) Simulated magnetic field (colour map) and electric field (black arrow) distributions inside the metamaterial absorber at the absorption peak wavelengths of samples with the GST film being in crystalline phase.

increase, as shown in Fig. 5(b). Interestingly, the position of the absorption peak S remains nearly invariant (as shown in Fig. 5(a)). Such behavior can be understood from different points of view. First, because the optical fields of the LSPR mode are mainly distributed in air, the resonance wavelength of such a mode is insensitive to the change in refractive index of the GST layer. Moreover, the temperature-induced change in the GST refractive index is also quite weak in the vicinity of the LSPR resonance wavelength, which explains why the peak S corresponding to LSPR almost does not move. Conversely, the peak F redshifts from 940 to 1410 nm in the phase-transition process, which is caused by the increase in the real part of the refractive index of the GST layer. Meanwhile, as the working bandwidth of the absorber is enlarged by about 470 nm in going from the amorphous to the crystalline state, the absorption efficiency decreases simultaneously. Such a phenomenon can be attributed to the mismatch between the radiative and absorptive quality (Q) factors of our device, which occur along with such a phase change,³⁷ since the increased imaginary part of the refractive index (k) of the GST layer in the phase-change process (see Fig. 5(b)) decreases the absorptive Q factor but leaves the radiative Q factor nearly unchanged. Fig. 5(c) depicts the distributions of magnetic and electric fields at two absorption peak frequencies for the sample in the cGST phase, showing similar features for resonance modes as those in the aGST phase (see Fig. 3). Therefore, the nature of the two resonance modes is unchanged for the metamaterial absorbers in the different phase states.

The working band of our metamaterial absorber can also be continuously modulated by tuning the GST film at an arbitrary intermediate phase with different ratios of amorphous and crystalline molecules, due to the dramatic change in the refractive

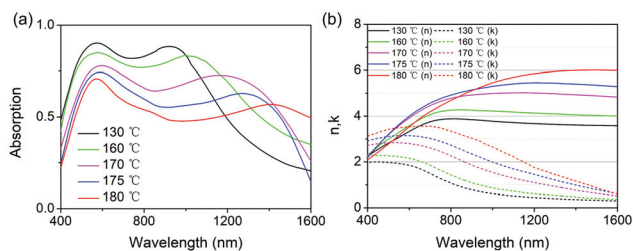


Fig. 6 (a) Measured absorption spectra of the broadband metamaterial absorbers fabricated with five different annealing temperatures. (b) Optical constants n (real part, solid lines) and k (imaginary part, dashed lines) of the GST film at different intermediate phases in five different samples.

index of GST. In our experiments, we successfully fabricated a series of metamaterial absorbers with GST layers at different intermediary phases through controlling the annealing temperature. In contrast with other kinds of volatile phase-change materials, such as VO_2 , GSTs at different phases are quite stable at room temperature, which is highly desirable for practical applications. Fig. 6(a) shows the measured absorption spectra of five different samples. The optical constants of the GST film at corresponding annealing temperatures were measured and are compared in Fig. 6(b), and are fully considered in our simulations. In the wavelength range 940–1600 nm, both the real and imaginary parts (n and k , respectively) of the refractive index of GST increase with temperature. As discussed previously, dictated by the FP resonance nature, the wavelength of peak F must be proportional to the refractive index n of the GST film, leading to redshifts in wavelength along with the temperature changes. Conversely, the LSPR-induced absorption peak S remains nearly unchanged during the transition process. Considering that the imaginary part of the refractive index k increases with the annealing temperature, the absorption Q factor of the device therefore decreases. Thus, the continuously decreasing absorptivity is due to the gradually mismatched radiation and absorption Q factors in our devices. Such a phenomenon means that our device gradually departs from the behavior of a broadband-perfect absorber. However, this issue may be resolved if the GST film is replaced by another phase-change material with weakly varying loss.

It should be noted that, since the reamorphization process of GST requires an annealing temperature above 640 °C, which is much higher than the melting point of the alumina, the proposed metamaterial absorbers cannot be changed from the crystalline state back to the amorphous state. If the alumina is replaced with other metals with higher melting point (such as tungsten and molybdenum),^{3,36} the proposed absorber can be reversibly switched from the amorphous state to the crystalline one.

Conclusions

In summary, we have experimentally demonstrated centimeter-scale, broadband, polarization-independent, and tunable

metamaterial absorbers, fabricated using a low-cost and lithography-free process with an AAO template. The fabricated samples exhibit high absorptivity (>80%) within a broad wavelength band ranging from 480 to 1020 nm, which merges two absorption peaks contributed by LSPR of the Al nanoparticles and FP resonances inside the spacer layers. Compared with previously realized broadband absorbers, which rely on dual or multiple resonances of the same type,^{11,17–19,42} here, the newly proposed device adopts two resonance modes with distinct origins, which can be tuned independently by structural optimizations. As a result, in such a simple configuration our device exhibits more flexibility in fitting diverse sensor application with different bandwidth requirements. In particular, the absorption band can be continuously tuned by thermally changing the phase state of the GST spacer layers inside the metamaterial absorbers. All these attractive characteristics are demonstrated by our optical experiments and full-wave simulations. Our work may stimulate many potential applications, such as solar cells, energy harvesting, smart sensing/imaging and color printing.

Conflicts of interest

There are no conflicts to declare.

Acknowledgements

This work was supported by National Key Research and Development Program of China (2017YFA0303500, 2017YFA0700201), National Natural Science Foundation of China (No. 11874118, 61675219, 61475173, 61875256, 11674068, 11734007, 91850101), Shanghai Science and Technology Committee (Grant No. 18ZR1403400), and Changchun Institute of Optics, Fine Mechanics and Physics, Chinese Academy of Sciences.

References

- 1 A. Tittl, A. U. Michel, M. Schäferling, X. Yin, B. Gholipour, L. Cui, M. Wuttig, T. Taubner, F. Neubrech and H. Giessen, *Adv. Mater.*, 2015, **27**, 4597–4603.
- 2 C. Zou, G. Ren, M. M. Hossain, S. Nirantar, W. Withayachumnankul, T. Ahmed, M. Bhaskaran, S. Sriram, M. Gu and C. Fumeaux, *Adv. Opt. Mater.*, 2017, **5**, 1700460.
- 3 K. Du, Q. Li, Y. Lyu, J. Ding, Y. Lu, Z. Cheng and M. Qiu, *Light: Sci. Appl.*, 2017, **6**, e16194.
- 4 T. Asano, M. Suemitsu, K. Hashimoto, M. De Zoysa, T. Shibahara, T. Tsutsumi and S. Noda, *Sci. Adv.*, 2016, **2**, e1600499.
- 5 Â. Carminati and K. Joulain, *Nature*, 2002, **416**, 61–64.
- 6 C. M. Watts, X. Liu and W. J. Padilla, *Adv. Mater.*, 2012, **24**, OP98–OP120.

- 7 N. Liu, M. Mesch, T. Weiss, M. Hentschel and H. Giessen, *Nano Lett.*, 2010, **10**, 2342–2348.
- 8 X. Liu, T. Tyler, T. Starr, A. F. Starr, N. M. Jokerst and W. J. Padilla, *Phys. Rev. Lett.*, 2011, **107**, 045901.
- 9 H. A. Atwater and A. Polman, *Nat. Mater.*, 2010, **9**, 865–865.
- 10 Y. Cui, K. H. Fung, J. Xu, H. Ma, Y. Jin, S. He and N. X. Fang, *Nano Lett.*, 2012, **12**, 1443–1447.
- 11 J. Zhu, Z. Ma, W. Sun, F. Ding, Q. He, L. Zhou and Y. Ma, *Appl. Phys. Lett.*, 2014, **105**, 021102.
- 12 N. I. Landy, S. Sajuyigbe, J. J. Mock, D. R. Smith and W. J. Padilla, *Phys. Rev. Lett.*, 2008, **100**, 207402.
- 13 T. V. Teperik, F. J. García de Abajo, A. G. Borisov, M. Abdelsalam, P. N. Bartlett, Y. Sugawara and J. J. Baumberg, *Nat. Photonics*, 2008, **2**, 299–301.
- 14 H. Tao, N. I. Landy, C. M. Bingham, X. Zhang, R. D. Averitt and W. J. Padilla, *Opt. Express*, 2008, **16**, 7181–7188.
- 15 J. Hao, J. Wang, X. Liu, W. J. Padilla, L. Zhou and M. Qiu, *Appl. Phys. Lett.*, 2010, **96**, 251104.
- 16 P. Yu, L. V. Besteiro, Y. Huang, J. Wu, L. Fu, H. H. Tan, C. Jagadish, G. P. Wiederrecht, A. O. Govorov and Z. Wang, *Adv. Opt. Mater.*, 2019, **7**, 1800995.
- 17 L. Huang, D. R. Chowdhury, S. Ramani, M. T. Reiten, S.-N. Luo, A. J. Taylor and H.-T. Chen, *Opt. Lett.*, 2012, **37**, 154–156.
- 18 K. Aydin, V. E. Ferry, R. M. Briggs and H. A. Atwater, *Nat. Commun.*, 2011, **2**, 517.
- 19 J. A. Bossard, L. Lin, S. Yun, L. Liu, D. H. Werner and T. S. Mayer, *ACS Nano*, 2014, **8**, 1517–1524.
- 20 C. Yang, C. Ji, W. Shen, K. Lee, Y. Zhang and X. Liu, *ACS Photonics*, 2016, **3**, 590–596.
- 21 S. Abedini Dereshgi, A. Ghobadi, H. Hajian, B. Butun and E. Ozbay, *Sci. Rep.*, 2017, **7**, 14872.
- 22 A. Ghobadi, S. A. Dereshgi, H. Hajian, B. Bozok, B. Butun and E. Ozbay, *Sci. Rep.*, 2017, **7**, 4755.
- 23 S. Thongrattanasiri, F. H. L. Koppens and F. J. García de Abajo, *Phys. Rev. Lett.*, 2012, **108**, 047401.
- 24 Z. Fang, S. Thongrattanasiri, A. Schlather, Z. Liu, L. Ma, Y. Wang, P. M. Ajayan, P. Nordlander, N. J. Halas and F. J. García de Abajo, *ACS Nano*, 2013, **7**, 2388–2395.
- 25 Z. Miao, Q. Wu, X. Li, Q. He, K. Ding, Z. An, Y. Zhang and L. Zhou, *Phys. Rev. X*, 2015, **5**, 041027.
- 26 M. A. Kats, R. Blanchard, S. Zhang, P. Genevet, C. Ko, S. Ramanathan and F. Capasso, *Phys. Rev. X*, 2013, **3**, 041004.
- 27 K. V. Sreekanth, S. Han and R. Singh, *Adv. Mater.*, 2018, **30**, 1706696.
- 28 Y. Meng, J. K. Behera, Y. Ke, L. Chew, Y. Wang, Y. Long and R. E. Simpson, *Appl. Phys. Lett.*, 2018, **113**, 071901.
- 29 C. Zhao, Y. Zhu, Y. Su, Z. Guan, A. Chen, X. Ji, X. Gui, R. Xiang and Z. Tang, *Adv. Opt. Mater.*, 2015, **3**, 248–256.
- 30 C. E. Petoukhoff and D. M. O'Carroll, *Nat. Commun.*, 2015, **6**, 7899.
- 31 Q. Hao, W. Li, H. Xu, J. Wang, Y. Yin, H. Wang, L. Ma, F. Ma, X. Jiang, O. G. Schmidt and P. K. Chu, *Adv. Mater.*, 2018, **30**, 1705421.
- 32 G. Wang, X. Chen, S. Liu, C. Wong and S. Chu, *ACS Nano*, 2016, **10**, 1788–1794.
- 33 L. Zhou, Y. Tan, D. Ji, B. Zhu, P. Zhang, J. Xu, Q. Gan, Z. Yu and J. Zhu, *Sci. Adv.*, 2016, **2**, e1501227.
- 34 B. Fang, C. Yang, C. Pang, W. Shen, X. Zhang, Y. Zhang, W. Yuan and X. Liu, *Appl. Phys. Lett.*, 2017, **110**, 141103.
- 35 W. Dong, Y. Qiu, J. Yang, R. E. Simpson and T. Cao, *J. Phys. Chem. C*, 2016, **120**, 12713–12722.
- 36 Y. Qu, Q. Li, K. Du, L. Cai, J. Lu and M. Qiu, *Laser Photonics Rev.*, 2017, **11**, 1700091.
- 37 C. Qu, S. Ma, J. Hao, M. Qiu, X. Li, S. Xiao, Z. Miao, N. Dai, Q. He, S. Sun and L. Zhou, *Phys. Rev. Lett.*, 2015, **115**, 235503.
- 38 W. Wang, Y. Qu, K. Du, S. Bai, J. Tian, M. Pan, H. Ye, M. Qiu and Q. Li, *Appl. Phys. Lett.*, 2017, **110**, 101101.
- 39 H. Wang and L. Wang, *Opt. Express*, 2013, **21**, A1078.
- 40 F. Ding, J. Dai, Y. Chen, J. Zhu, Y. Jin and S. I. Bozhevolnyi, *Sci. Rep.*, 2016, **6**, 39445.
- 41 X. Chen, H. Gong, S. Dai, D. Zhao, Y. Yang, Q. Li and M. Qiu, *Opt. Lett.*, 2013, **38**, 2247–2249.
- 42 N. Mou, S. Sun, H. Dong, S. Dong, Q. He, L. Zhou and L. Zhang, *Opt. Express*, 2018, **26**, 11728–11736.
- 43 H. Ullah, A. D. Khan, M. Noman and A. U. Rehman, *Plasmonics*, 2018, **13**, 591–597.
- 44 H. Liu, Z. H. Wang, L. Li, Y. X. Fan and Z. Y. Tao, *Sci. Rep.*, 2019, **9**, 5751.
- 45 L. Ding, X. Luo, L. Cheng, M. Thway, J. Song, S. J. Chua, E. E. M. Chia and J. Teng, *Adv. Opt. Mater.*, 2018, **6**, 1800928.
- 46 K. Du, L. Cai, H. Luo, Y. Lu, J. Tian, Y. Qu, P. Ghosh, Y. Lyu, Z. Cheng, M. Qiu and Q. Li, *Nanoscale*, 2018, **10**, 4415–4420.